ISSN: 1813-4890

Finite element simulation and experimental validation of laser cutting of chromium-molybdenum steel thin plates without assistant gas

Zhen Sun, Lin Zhong, Lei Chen

School of Mechatronic Engineering, Southwest Petroleum University, Chengdu 610500, China

Abstract

Remote laser cutting provides a feasible solution for the safe and efficient disposal of short sections of wellheads in oil and gas well fire rescue, but the high-temperature environment at the site requires the use of a remote approach, which makes it impossible to remove the slag from the cut seam by using auxiliary blowing gas. The purpose of this study is to explore the influence of laser process parameters on the temperature field and slit depth of chromium-molybdenum (Cr-Mo) steel sheet under the environment without assistant gas. By establishing a 2D finite element model for laser cutting under unassisted gas, coupling heat transfer and fluid properties, and tracking the three-phase interfaces of solid, liquid, and gas by using the level-set method, we simulate the effects of moving speed, laser power, and focal length on the cutting depth. Subsequently, a one-factor experiment is carried out with a 20CrNiMo thin steel plate as a specimen to validate the model. The results show that the laser parameters have a significant effect on the cutting temperature field and the cutting depth under the condition of no auxiliary gas, and the experimental results verify the accuracy of the model. This study provides theoretical guidance for laser cutting of Cr-Mo steel plate under the environment of unassisted gas, and also provides reference for the optimization of cutting process parameters and the design of laser cutting scheme for thick-walled tubing at the wellhead in the subsequent development.

Keywords

Unassisted gas; Laser cutting; Finite element simulation; Experimental validation.

1. Introduction

The environment of oil and gas well fire rescue site is complex and harsh, often accompanied by high temperature, flammable gas aggregation and other dangerous factors. In such emergency situations, quickly cutting off the wellhead tubing column and blocking the oil and gas ejection channel are the key links to control the danger and protect personnel safety [1-4]. Traditional mechanical cutting relies on close-range operation and low efficiency; plasma arc cutting is prone to produce sparks and fumes that cause secondary risks; abrasive water jet (AWJ) cutting is inefficient and difficult to implement, and it is difficult to balance efficiency, safety and convenience, and it is unable to meet the needs of field scenarios. In contrast, laser cutting technology has good focusing performance and high power density, can realize the long-distance precision cutting of metal pipes, significantly reducing the operational risk of rescue personnel, the technology has been widely used in aerospace, automotive manufacturing and energy engineering and other field [5-9]. Therefore, laser cutting technology, with its unique advantages, is expected to become an important means of realizing efficient and safe cutting operations in oil and gas well fire rescue [10-12].

Chen et al. analyzed the effect of different amount of defocus on the cutting effect through laser cutting experiments of 20mm thick 20CrNiMo steel plate under different amount of defocus,

ISSN: 1813-4890

revealed the effect of defocus on the cutting performance of thick steel, and verified the technical feasibility of unassisted blowing to cut thick steel [13]. Liao et al. carried out unit cutting experiments for the same conditions (unassisted air blowing, 20mm thick 20CrNiMo steel plate), and found that the wide kerf width and top-down cutting path help slag discharge, which further confirms the feasibility of cutting medium-thickness steel plate with a high-power laser without assisted air [14]. Wandera et al. used a 4kW laser to cut a 10mm stainless steel plate and achieved slag-free cutting edges by reducing the cutting speed, focusing the laser beam with a long focal length lens and locating the focal point on the bottom surface of the workpiece, while reducing the surface roughness and vertical deviation of the cutting edges. [15]. Manohar et al. showed that steel composition, especially carbon, sulphur, silicon and alloying elements, significantly affects the quality and stability of laser cutting of 25 mm thick steel plates by changing the thermophysical properties [16]. Tamura et al. demonstrated that a 30kW fiber laser can efficiently cut steel plates up to 300 mm thick and complex simulated nuclear components, providing a viable solution for processing thick sections in decommissioning nuclear facilities [17]. Liu et al. investigated the material removal mechanism of high-power fiber laser cutting of thick carbon steel, and the study proposed a process optimization scheme for quality problems such as slag adhesion and roughness at the bottom of the slit to improve cutting quality and efficiency [18]. Wang et al. established a multiphase flow coupling model for fiber laser cutting simulation, experimentally verified the accuracy of the model, and revealed the material microscopic removal mechanism, which can reduce the problems of stent forming and provide an optimized process solution for fiber laser cutting [19]. Vora et al. designed and developed a multi-step computational model based on COMSOL Multiphysics, integrating heat transfer, fluid dynamics boundary conditions, and thermodynamic properties to predict surface roughness under various laser processing conditions. The predictions exhibited strong agreement with experimental observations [20]. Parandoush et al. reviewed the modeling and simulation of laser beam machining, noting that both physics-based and artificial intelligence-based models can be employed to predict quality characteristics within a given range of input parameters and to determine the optimal process window [21]. Faraji et al. proposed a three-dimensional finite-volume numerical model to simulate fluid flow, heat transfer, and mass transfer during both similar and dissimilar laser welding of Ti-6Al-4V and Inconel 718, the simulated weld pool shapes and dimensions demonstrated high consistency with experimental results, confirming the model's effectiveness [22]. Singh et al. developed a finite element model of laser-assisted machining of AISI D2 tool steel, the model predicted temperature distribution, flow stress reduction due to laser heating, and cutting forces with less than 8% error compared to literature data [23]. Čepauskaitė et al. analyzed the influence of fiber laser process parameters (laser power, cutting speed and auxiliary gas pressure) on the cutting accuracy of thin (4 mm) and thick (6 mm) S355JR steel plates, they combined experimental analysis with artificial neural network modelling to propose parameter optimization methods for surface roughness, dimensional accuracy and cut taper [24]. Buj-Corral et al. investigated the influence of laser process parameters on the cut quality of stainless steel thin plates, the study addressed the problem of optimizing parameter selection to improve laser cutting precision and surface finish by statistically analyzing surface roughness, kerf geometry, and dimensional accuracy [25]. PRAMANIK et al. examined the effect of cutting angle in low-power fiber laser cutting of thin 316L stainless steel, addressing the challenge of optimizing kerf geometry, surface roughness, and heat-affected zone for improved precision [26]. Overall, existing research mostly focuses on the application of high-power laser in medium-thickness plate cutting, with the material types of aluminum alloy, stainless steel and carbon steel as the main materials, and the results are mainly focused on the quality of the cut seam, and the research on low-power laser cutting of Cr-Mo steel thin plate is relatively insufficient, especially the influence of the laser parameter on the temperature field and the

ISSN: 1813-4890

depth of the cut seam under the condition of no auxiliary gas, the experiments and modeling are still imperfect, and the systematic optimization of the process parameter and cutting mechanism are lacking and cutting mechanism analysis.

Based on the above background, this study aims to systematically investigate the process characteristics of low-power laser cutting of Cr-Mo steel thin plates without assist gas by combining experimental methods with finite element simulations, focusing on analyzing the effects of cutting speed, laser power and focal length on cutting depth and slag removal mechanisms. The findings are expected to provide both theoretical and practical support for process optimization as well as for remote cutting of thick-walled wellhead pipes in field applications.

2. Methods

This study systematically analyzes the influence of laser process parameters on the cutting depth of Cr-Mo steel thin plate under the condition of no auxiliary gas by combining finite element simulation and experimental verification. The research methods are specified as follows:

(1) Finite element modeling: A 2D finite element model is established to simulate the effects of laser power, moving speed and focal length on Cr-Mo steel plate for analysis, to reveal its role in the cutting depth and the behavior of material removal.

(2) Experimental validation: Carry out single-factor experiments to obtain the actual effects of parameters on the cutting depth with a 20CrNiMo thin plate as a specimen to verify the reliability and applicability of the model.

2.1. Modeling

2.1.1. Evolution of surface morphology

In the process of laser cutting Cr-Mo steel plate, the laser beam is focused on the surface of the steel plate, and the high energy is rapidly transferred to the local area, which makes the surface rapidly heat up and reach the melting temperature. The laser forms a high-temperature melting pool on the surface of the steel plate, and the local temperature rises sharply, generating a strong thermal gradient, which makes the metal tissue in the melting pool undergo rapid liquefaction and volatilization. With the continuous input of laser energy, the molten pool appears more intense convection movement, the liquid melt vaporization intensity increases, the vaporization steam will produce a greater recoil pressure on the melt, when the recoil pressure of the vaporized steam of molten chromium molybdenum steel is greater than the surface tension of the liquid melt, Cr-Mo steel liquid will be separated, broken or even splash. When the laser beam leaves the cutting area or the energy input is reduced, the molten pool begins to cool and solidify rapidly. The rapid reduction in temperature allows the metal to be transformed from a liquid to a solid in a short period of time. The laser cutting process can be described by the most basic heat transfer equation, which is also the equation of conservation of energy for the interaction of the laser with the material, as shown in the following equation [13]:

$$\rho C_P \left[\frac{\partial T}{\partial t} + u \cdot \nabla T \right] = \nabla \cdot (k \nabla T) + \alpha I \tag{1}$$

where T is the temperature field distribution of the material, ρ is the density of the material, C_p is the specific heat capacity of the material, u is the velocity field distribution of the material, k is the thermal conductivity of the material, α is the absorption coefficient of the material and I is the laser heat source.

ISSN: 1813-4890

In this study, the finite element simulation software COMSOL was used to establish a two-dimensional finite element computational model combining heat transfer and fluid properties with the aim of quantitatively analyzing the trend of the depth of cut gradient under laser power, moving speed and focal length. As shown in Fig. 1, the size of the model is 10 mm × 5 mm, and the laser moves along the x-axis direction on the upper surface of the model, which is meshed with free triangles, with the maximum and minimum mesh sizes of 50μm and 20μm, respectively, and mesh refinement in the region close to the laser movement.

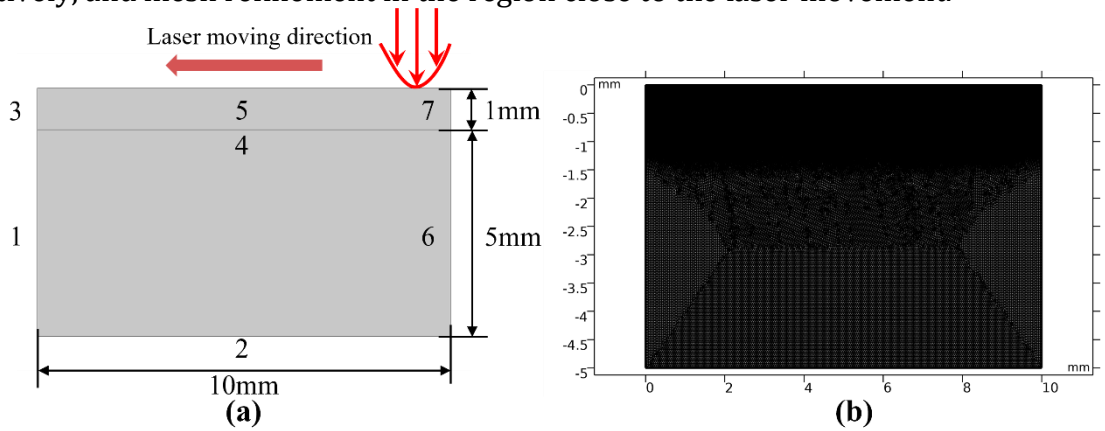

Fig. 1. Finite element computational model: (a)2D computational model, (b) mesh partitioning of the model.

The cutting process of the laser is regarded as a moving heat source, and its energy distribution is described by the Gaussian surface heat source model to simulate the spatial attenuation characteristics of the laser beam energy in the cutting process in the form of the following equation:

$$I = \frac{AP}{\pi r_0^2} \exp\left[-B\left(\frac{x-vt}{r_0}\right)^2\right] \tag{2}$$

where I is the heat flux density at a distance of r_0 from the center of the heat source; A is the material absorption coefficient for the laser; P is the power density; B is the shape factor of the Gaussian distribution of the heat flux; r_0 is the radius of the laser spot and v is the moving speed of the laser spot. The parameters used in the laser cutting model with different parameters are shown in Table 1.

Table 1. Laser cutting simulation parameters.

Laser Parameters	Value (units)
Power(W)	500, 700, 900, 1100, 1300
Focal length (mm)	-10, -8, -4, 0, 4
Cutting Speed (mm/s)	6, 10, 16, 20, 24

2.1.2. Simulation of kerf morphology

In order to further simulate the geometrical topography after cutting, this study introduces the level set method in the finite element model for tracking the interfacial transformation of Cr-Mo steel plate between solid, liquid and gas phases [20]. Through the phase transition governing equations combined with the boundary conditions, the transformation process of the material from solid to liquid and then to gas at different temperatures is described, so as to more realistically reproduce the formation mechanism of the cuts. The method not only reflects the melting and vaporization processes, but also provides a reliable numerical basis for the depth and morphology analysis of the cut seam. The parameter B reported in Table 2 corresponds to the level-set–based volume fraction field used to represent the three coexisting phases. When T_x=T_m , B is interpreted as the liquid-phase volume fraction in relation to the solid

ISSN: 1813-4890

phase: B=0 denotes a completely solid material (100% solid), B=1 denotes a completely molten material (0% solid), and intermediate B values indicate partially melted states. Similarly, when T_x reaches the gasification (vaporization) temperature T_v, B expresses the gaseous-phase volume fraction versus the liquid; B=0 corresponds to an entirely liquid region while B=1 denotes a fully gaseous region (no liquid present). Fractional B values between 0 and 1 therefore characterize two-phase mixtures (liquid + gas). In this regime the numerical model preserves only the solid-phase portion and computes the slit geometry accordingly.

Table 2. Heat transfer equations and boundary conditions for the 2D model.

Boundary No.	Boundary condition	Equation
Whole geometry	Temperature-dependent specific heat	$C_{p1} = C_p + \delta_m(L_m) + \left(\frac{L_m}{T_m}\right) \cdot H'((T - T_m))\Delta T$ $+\delta_V(L_V) + \left(\frac{L_V}{T_V}\right) \cdot H'\left((T - T_V), \Delta T\right)$ $\delta_m = \exp\left(-\left((T - Tm)^2 / \Delta T^2\right)\right) / \Delta T\sqrt{\pi},$ $\delta_v = \exp\left(-\left((T - T_V)^2 / \Delta T^2\right)\right)$
Whole geometry	Governing equation	$\rho C_p\left(\frac{\partial T}{\partial t}\right) = \nabla \cdot (k \nabla T)$
4	Heat flux model Natural convection cooling and radiation	$I = \frac{AP}{\pi r_0^2} \exp\left[-B\left(\frac{x - vt}{r_0}\right)^2\right]$ $-k\frac{\partial T}{\partial y} = \beta P - h(T - T_\alpha) - \varepsilon\sigma(T^4 - T_\alpha^4)$
1，3，5，6，7	Natural convection cooling and radiation	$-k\frac{\partial T}{\partial y} = h(T - T\alpha) - \varepsilon\sigma\left(T^4 - T_\alpha^4\right),$ $-k\frac{\partial T}{\partial x} = h(T - T\alpha) - \varepsilon\sigma\left(T^4 - T_\alpha^4\right)$
Whole geometry	Level set method	$B = 1 \ \text{for}(T > T_x + \Delta T)$ $B = \frac{(T - T_x + \Delta T)}{2\Delta T} \ \text{for}(T_x - \Delta T) \le T \le (T_x + \Delta T)$ $B = 0 \ \text{for}(T < T_x - \Delta T)$

2.2. Experiments

2.2.1. Experimental equipment and platform

In this study, a laser cutting experimental platform was built as shown in Fig. 2(a), which mainly includes: a continuous laser, a laser cutting head, a moving platform, a drive controller, a water-cooling device and a vacuum cleaner. Among them, the laser adopts SMATLas 4S series single-mode continuous fiber laser produced by Guanghui (Shanghai) Laser Science and Technology Co., Ltd. and the laser cutting head has an adjustable focal length range of -20mm~20mm, an output wavelength of 1080nm, an output power of 1,500W, and a power density of up to 24,000KW/mm^2. In the experimental process, the laser head is fixed on the platform stationary, through the calculator on the drive controller to control, realize the moving platform in the horizontal direction and vertical direction of the uniform speed movement, so as to drive the specimen to move to achieve cutting, the laser moving speed changes through the moving platform to drive the specimen to achieve. Since the experiment is carried out without auxiliary gas, in order to cool the cutting device, the laser cutting head is only connected to the water-

ISSN: 1813-4890

cooling device. A ContourGT InMotion 3D optical microscope is shown in Fig. 2(b), when the cutting experiment is completed on the specimen cut seam morphology, depth and other high-precision measurements, for different laser parameters under the depth of the cut seam of the comparative analysis.

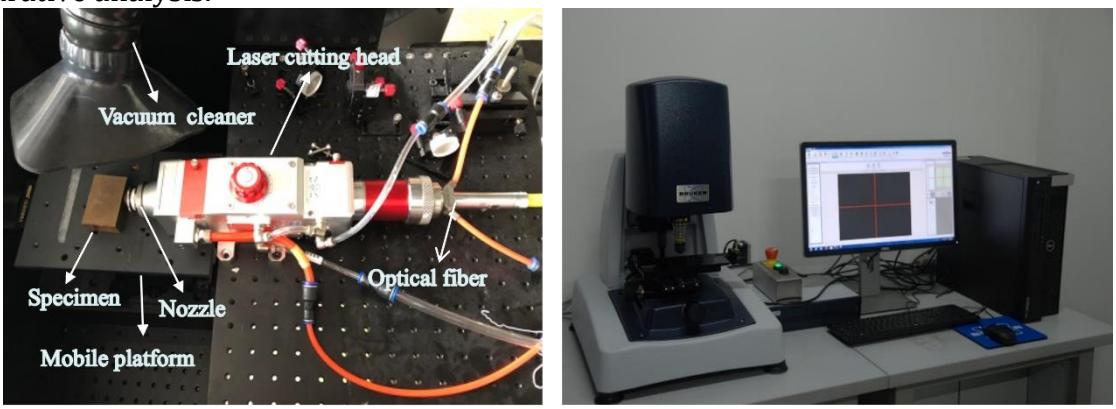

Fig. 2. Experimental equipment: (a) cutting experiment platform, (b) three-dimensional optical microscope.

2.2.2. Experimental program and parameters

In order to ensure that the results of the unit experiment are in line with the actual situation of the wellhead, the experimental specimen is made of Cr-Mo steel (20CrNiMo steel), which is consistent with the tubing of the oil and gas wellhead, and its chemical composition is shown in Table 3, and the dimensions of the specimen used in the unit experiment are 30 mm × 5 mm × 10 mm.

Table 3. The material composition of 20CrNiMo is as follows.

Composition	C	Si	Mn	P	S	Cr	Ni	Cu
Quality percentage/%	0.37~0.44	0.17~0.37	0.60~0.90	≤0.04	≤0.05	≤0.25	≤0.25	≤0.25

Through single-factor experiments, the laser cutting speed, power and focal length were tested for their influence on cutting depth, and the influence laws of the three laser parameters were obtained. Due to the complexity of the environment at the wellhead accident site, the slag generated during the cutting process cannot be removed by blowing when the laser cuts the thick-walled tubing at the wellhead at a long distance. In order to ensure a better cutting effect without blowing, the specimen is designed with a slit width of 5mm, and the specimen is placed vertically relying on the platform to reciprocate and move upward by 0.1mm in the vertical direction for every one cycle of reciprocating motion. The schematic diagram of the cutting method and the slit are shown in Fig. 3. After the completion of the laser cutting specimen, through the three-dimensional optical microscope on the depth of the slit for high-precision measurements, in order to reduce the measurement error, in a slit were taken in five areas for detection and the results will be organized and plotted as a box plot, the average value of each group of data is plotted as a folded line graph. The schematic diagram of the experimental measurement is shown in Fig. 4.

ISSN: 1813-4890

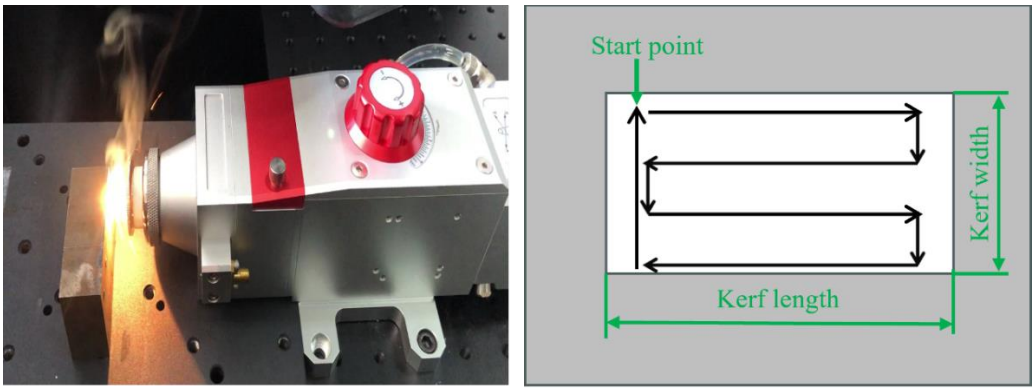

Fig. 3. Experimental design: (a) laser cutting process, (b) cutting path.

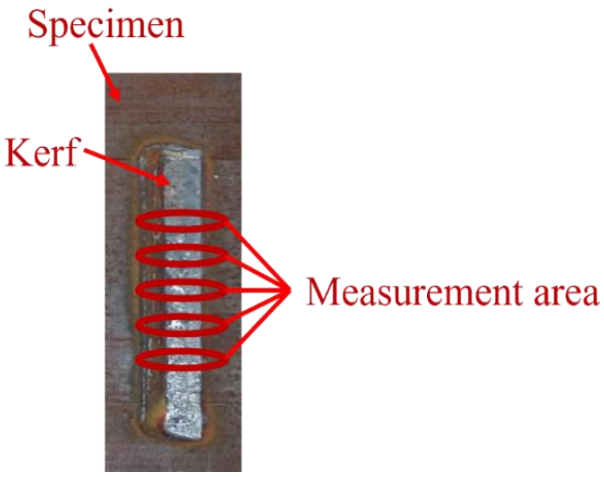

Fig. 4. Measurement area.

3. Results and discussions

3.1. Effect of cutting speed

At a laser power of 900 W and a focal distance of -4 mm, the simulated cutting depths and corresponding experimental measurements of the Cr-Mo steel plate under different laser scanning speeds are summarized in Table 4. At a cutting speed of 6 mm/s, the variance of the kerf depth reaches its maximum value (0.0009), indicating pronounced fluctuations in cutting depth at this condition. The maximum error rate is observed to be 5.15%. These results indicate that when the scanning speed is treated as a variable, the discrepancy between the simulated and experimental cutting depths remains relatively small. Overall, the model demonstrates strong consistency with the experimental data within the cutting speed range of 6–24 mm/s.

Table 4. Simulated and experimentally measured values of cutting depth at different travelling speeds.

Cutting speed(mm/s)	Simulation depth(mm)	Experimental test depth (mm)					variance	Error ratio (%)
6	1.1205	1.0587	1.1297	1.1402	1.1317	1.0887	0.0009	0.95
10	0.8302	0.8082	0.8324	0.8568	0.8442	0.8204	0.0002	0.26
16	0.6843	0.6596	0.6988	0.7102	0.6568	0.6401	0.0007	1.63
20	0.4053	0.3584	0.3927	0.3821	0.4102	0.3787	0.0002	5.15
24	0.1345	0.1377	0.1483	0.1389	0.1239	0.1162	0.0001	1.11

ISSN: 1813-4890

Taking the laser cutting speed of 6 mm/s as an example, the simulated cutting depth and the corresponding experimental measurements are shown in Fig. 5(a),5(b) and 5(c). It can be observed that as the laser cutting speed increases from 6 mm/s to 24 mm/s, the cutting depth decreases significantly. This is because an excessively high scanning speed prevents the material from undergoing complete melting and expulsion from the kerf, resulting in molten material accumulating within the kerf and thereby reducing the cutting depth. At a cutting speed of 6 mm/s, the laser interacts with the specimen surface for a longer duration compared with 20 mm/s and 24 mm/s, allowing the specimen to adequately absorb the laser energy, undergo full melting, and discharge molten material under the influence of gravity. As the cutting speed increases, the laser residence time per unit area of the specimen decreases, leading to insufficient absorption of laser energy and incomplete melting of the specimen surface, which hinders the formation of a kerf. Consequently, higher laser cutting speeds correspond to shallower cutting depths. The difference between the experimental measurements and the simulated results may be due to the change in the parameters of the specimen during the laser cutting process. In addition, power fluctuations and slight focal deviations during the experiment could also influence the results.

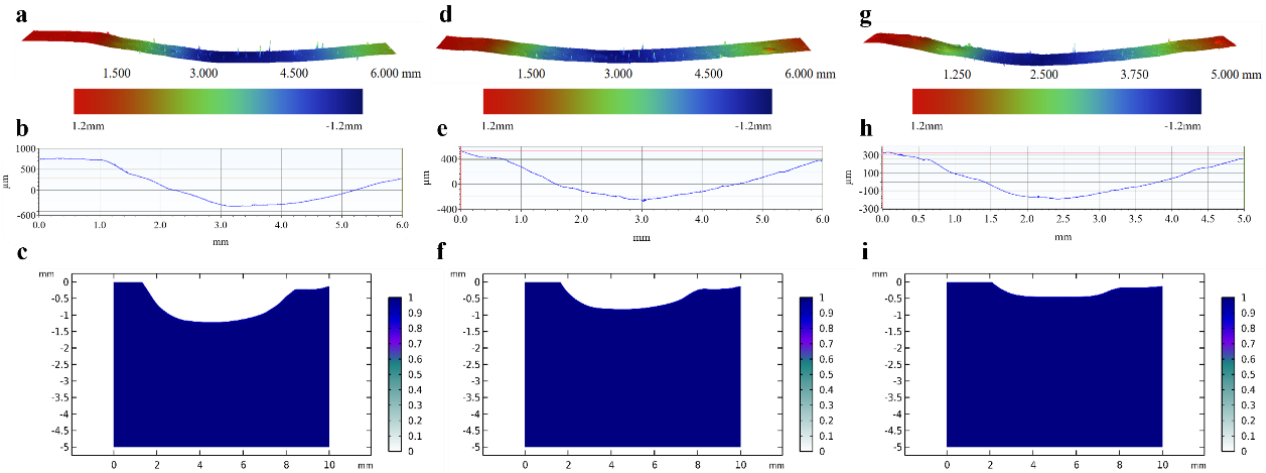

Fig. 5. Model predictions and experimental measurements of cutting depth.

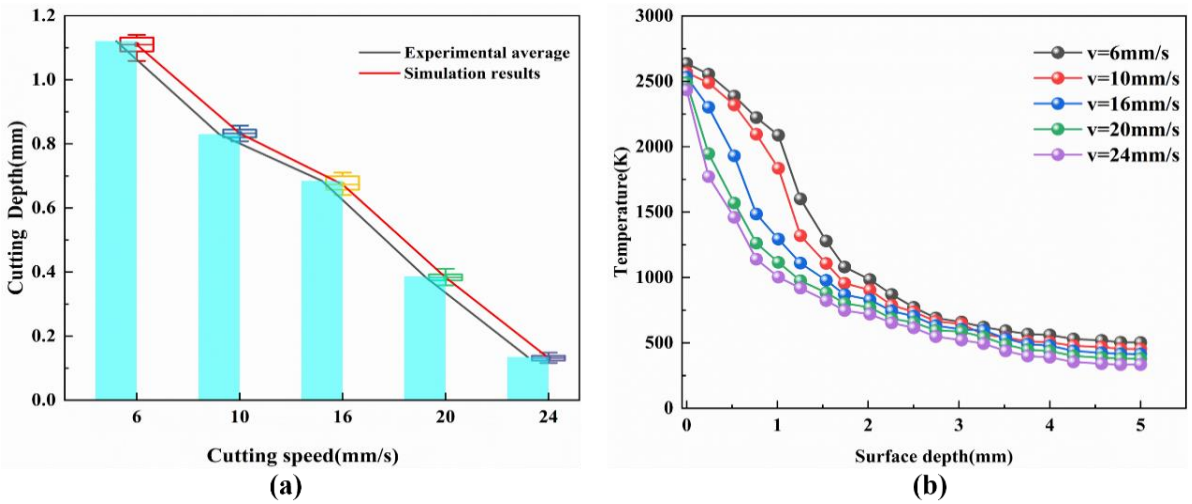

Fig. 6. Effect of laser cutting speed: (a) cutting depth, (b) temperature.

As shown in Fig. 6(a), both the experimental and simulated curves exhibit a monotonically decreasing trend of cutting depth with increasing scanning speed, thereby validating the accuracy of the model. It further reveals differences in the temperature field distribution in Fig. 6(b): under low-speed conditions, the laser generates a broad high-temperature zone on the

ISSN: 1813-4890

surface and subsurface of the specimen, with the peak temperature approaching the vaporization threshold, which facilitates the smooth removal of molten material under the action of gravity. In contrast, at higher speeds, the shortened thermal interaction time leads to a sharp reduction in peak temperature, confined only to the surface layer, resulting in insufficient fluidity of the molten metal and a subsequent decrease in cutting depth. These results indicate that an appropriately reduced scanning speed ensures adequate heat input and efficient expulsion of molten material, thereby enabling the formation of deeper kerfs.

3.2. Effect of laser power

At a laser cutting speed of 10 mm/s and a focal distance of -4 mm, the simulated cutting depths and the corresponding experimental measurements of the Cr-Mo steel plate under different laser powers are presented in Table 5. When the laser power was 500 W, the variance of the cutting depth reached its maximum value (0.0009), indicating relatively large fluctuations in depth at this condition. In addition, the maximum error rate was 1.37%. These results suggest that when laser power is considered as the variable, the model provides accurate predictions of the cutting depth.

Table 5. Simulated and experimentally measured values of cutting depth at different laser powers.

Laser power(W)	Simulation depth(mm)	Experimental test depth (mm)					variance	Error ratio (%)
500	0.7382	0.7201	0.7507	0.7605	0.7430	0.7085	0.0003	1.37
700	0.8061	0.7889	0.8042	0.8074	0.8107	0.7946	0.0001	0.62
900	0.8443	0.8289	0.8323	0.8568	0.8492	0.8174	0.0002	0.87
1100	0.9652	0.9436	0.9685	0.9638	0.9743	0.9324	0.0002	0.14
1300	0.8571	0.8489	0.8697	0.8723	0.8551	0.8564	0.0001	0.36

When the laser power is 500 W, the simulated cutting depth and the corresponding experimental measurements are shown in Fig. 5(d), 5(e) and 5(f). It can be observed that laser power exerts a considerable influence on the cutting depth, with pronounced differences across the five tested power levels, primarily due to the accumulation of molten material within the kerf. As the laser power increased from 500 W to 1100 W, the cutting depth gradually increased, indicating that the molten material generated at these power levels could be effectively expelled under the action of gravity. However, at 1300 W, the cutting depth decreased, which was mainly attributed to excessive molten material accumulating inside the kerf. Laser power of 500 W, the specimen absorbs laser energy and generated a small amount of molten material; due to the relatively low power, the molten material produced was limited and could be expelled in a timely manner. With increasing power, the specimen absorbed more laser energy, producing greater quantities of molten material, which, once expelled, contributed to a deeper kerf. When the laser power is 1300 W, however, the specimen absorbed significantly more energy, resulting in excessive molten material. In the absence of an assist gas, molten material could only be removed by gravity, and the relatively slow expulsion rate caused large amounts of molten material to accumulate in the kerf, thereby reducing the cutting depth.

ISSN: 1813-4890

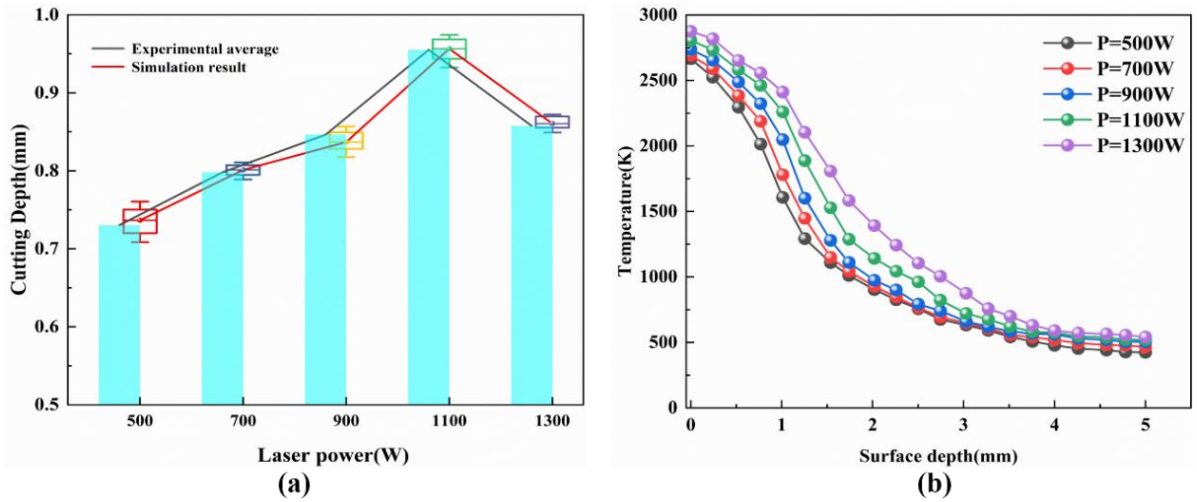

Fig. 7. Effect of laser power: (a) cutting depth, (b) temperature.

It clearly illustrates this trend in Fig. 7(a): within the range of 500–1100 W, the cutting depth increases with power, whereas at 1300 W, the depth decreases markedly. The temperature field distribution shown in Fig. 7(b) corresponds to this behavior. At low to medium power levels, the depth of the heat-affected zone expands with increasing power, which facilitates cutting by enabling the smooth expulsion of molten material. However, at 1300 W, although the peak temperature reaches its maximum, thermal accumulation leads to excessive molten material buildup, thereby reducing cutting efficiency. These results demonstrate that the relationship between laser power and cutting depth is non-monotonic, first increasing and then decreasing. Within an appropriate power range, both the molten depth and the extent of the high-temperature zone can be significantly enhanced, whereas excessively high power is constrained by molten material accumulation, ultimately limiting cutting efficiency.

3.3. Effect of focal length

At a laser power of 900 W and a cutting speed of 10 mm/s, the simulated cutting depths and corresponding experimental measurements of the Cr-Mo steel plate under different focal distances are presented in Table 6. When the focal distance is 4 mm, the variance of the kerf depth reaches its maximum value (0.0003), indicating relatively large fluctuations in depth under this condition. In addition, the maximum error rate is 3.21%. These results suggest that when focal distance is treated as the variable, the model exhibits only minor deviations in predicting cutting depth.

Table 6. Simulated and experimentally measured values of cutting depth at different focal lengths.

Focal length(mm)	Simulation depth(mm)	Experimental test depth (mm)					variance	Error ratio (%)
4	0.6501	0.6432	0.6746	0.6938	0.6506	0.6627	0.0003	2.29
0	0.9723	0.9639	0.9778	0.9928	0.9875	0.9697	0.0001	0.62
-4	0.8425	0.8122	0.8523	0.8368	0.8492	0.8204	0.0002	0.99
-8	0.4686	0.4757	0.4850	0.4924	0.4598	0.4616	0.0001	1.34
-10	0.4205	0.4214	0.4521	0.4465	0.4371	0.4129	0.0002	3.21

When the focal length is -10 mm, the simulated cutting depth and the corresponding experimental measurements are shown in Fig. 5(g), 5(h) and 5(i). As illustrated in the figure, the maximum cutting depth of 0.9723 mm is obtained at a focal distance of 0. When the focal length is not 0, the cutting depths varied significantly due to the influence of molten material

ISSN: 1813-4890

accumulation. The main reason is that when the focal distance is 0, the laser focal point is located exactly on the specimen surface, where the laser spot diameter is minimized and the power density reaches its maximum, enabling the specimen to absorb more energy per unit area. When the focal distance is positive, the laser focal point lies above the specimen surface; when it is negative, the focal point lies below the surface. In both cases, the laser spot diameter on the specimen surface increases relative to that at zero focal distance, resulting in a reduced power density and a lower energy absorption per unit area. Consequently, the melting rate of the material decreases, and at a scanning speed of 10 mm/s, part of the material fails to fully melt, leading to molten material accumulating in the kerf and ultimately reducing the cutting depth.

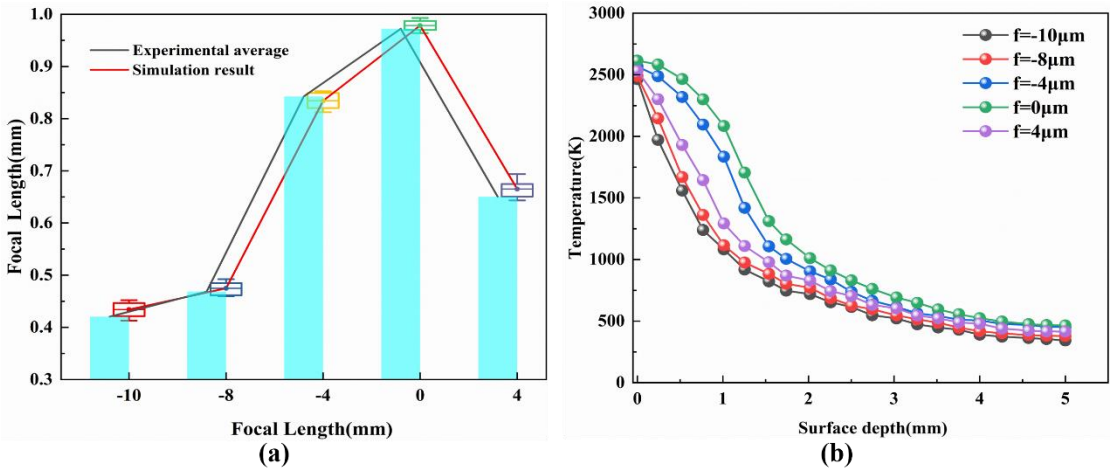

Fig. 8. Effect of focal length: (a) cutting depth, (b) temperature.

It clearly shows in Fig. 8(a) that the cutting depth peaks at a focal length of 0 mm, which is consistent with the experimental and simulation results; while the depth decreases at both positive and negative offsets. The temperature in Fig. 8(b) further illustrates this phenomenon: when the focal length is 0, the spot is the smallest, the power density is the largest, and the melting efficiency is the highest, which is conducive to the formation of a deep slit; when the focal length is deviated from the focal length, the spot disperses leading to the attenuation of the power density, the high temperature zone is narrowed and dispersed, and the melting speed decreases, which makes it difficult to discharge slag adequately, and the cutting depth thus decreases. It can be seen that the focal length has a significant effect on the cutting depth and temperature field, and the best cutting performance is achieved when the focal length is 0, while the focal point deviation will weaken the power density and heat input, resulting in a reduction in the cutting depth.

4. Conclusion

This study established a 2D finite element model for laser cutting of Cr-Mo steel plates without assist gas and validated through experiments. The model systematically revealed the influence of low-power laser parameters (laser power, cutting speed, and focal length) on cutting depth and molten material expulsion mechanisms under assist-gas-free conditions. The major outcomes of this study are presented as follows:

(1) The results of finite element prediction are confirmed by unit experiments and the error rate is within 6%, which proves that the proposed two-dimensional model can predict the cutting depth better, and has good reliability and engineering application value.

(2) When the moving speed is 6mm/s, the laser action time is sufficient, the material is melted thoroughly and the slag is discharged smoothly, and the cutting depth is maximum; with the

ISSN: 1813-4890

speed increasing to 24mm/s, the material is not melted sufficiently, and the cutting depth is significantly reduced.

(3) The effect of laser power on the cutting depth shows a non-monotonic trend: in the range of 500~l100W, with the increase of power, the material is fully melted and the slag can be discharged by gravity, and the cutting depth increases gradually; however, when the power rises to 1300W, the excessive accumulation of slag hinders the cutting, resulting in the depth of depth instead of decreasing.

(4) The focal length of 0 (the focus is located on the surface of the material), the laser power density is the highest, the material absorbs the most energy, the cutting depth is the largest. Under both positive and negative defocusing, the spot diameter increases, leading to reduced power density and consequently shallower cuts.

This study not only provides a systematic process parameter optimization basis for low-power laser cutting without auxiliary gas, but also has a guiding significance for the long-distance cutting program of thick-walled tubing at the wellhead.

References

[1] Han, C., Yang, X., Zhang, J., & Huang, X. (2015). Study of the damage and failure of the shear ram of the blowout preventer in the shearing process. Engineering Failure Analysis, 58, 83-95.

[2] Liu, Y., Zhang, S., Zhao, Y., & Ren, Z. (2022). Experiments on the kerf quality characteristic of mild steel while cutting with a high-power fiber laser. Optics & Laser Technology, 154, 108332.

[3] Tamura, K., Ishigami, R., & Yamagishi, R. (2016). Laser cutting of thick steel plates and simulated steel components using a 30 kW fiber laser. Journal of Nuclear Science and Technology, 53(6), 916-920.

[4] Su, X., Zhang, P., & Huang, Y. (2024). Research Progress of Metal Additive Manufacturing Technology and Application in Space: A Review. Metals, 14(12), 1373.

[5] Piscopo, G., & Iuliano, L. (2022). Current research and industrial application of laser powder directed energy deposition. The International Journal of Advanced Manufacturing Technology, 119(11), 6893-6917.

[6] Perka, A. K., John, M., Kuruveri, U. B., & Menezes, P. L. (2022). Advanced high-strength steels for automotive applications: Arc and laser welding process, properties, and challenges. Metals, 12(6), 1051.

[7] Shin, J. S., Ock, J., & Choi, S. (2025). Laser cutting study of zirconium alloys for nuclear decommissioning. Nuclear Engineering and Technology, 57(2), 103184.

[8] Vasanth, S., Muthuramalingam, T., Prakash, S. S., & Raghav, S. S. (2023). Investigation of SOD control on leather carbonization in diode laser cutting. MATERIALS AND MANUFACTURING PROCESSES, 38(5), 544-553.

[9] Nagalingam, A. P., Shamir, M., Tureyen, E. B., Sharman, A. R. C., Poyraz, O., Yasa, E., & Hughes, J. (2025). Recent progress in wire-arc and wire-laser directed energy deposition (DED) of titanium and aluminium alloys. The International Journal of Advanced Manufacturing Technology, 136(5), 2035-2073.

[10] Staudt, T., Tenner, F., Klämpfl, F., & Schmidt, M. (2017). Development of a hyperspectral imaging technique for monitoring laser-based material processing. Journal of Laser Applications, 29(2).

[11] Shin, J. S., Oh, S. Y., Park, H., Chung, C. M., Seon, S., & Kim, T. S., et al. (2018). Laser cutting of steel plates up to 100mm in thickness with a 6-kw fiber laser for application to dismantling of nuclear facilities. Optics and Lasers in Engineering, 100, 98-104.

[12] Shin, J. S., Oh, S. Y., Park, S. K., Park, H., & Lee, J. (2021). Improved underwater laser cutting of thick steel plates through initial oblique cutting. Optics & Laser Technology, 141, 107120.

[13] Chen, Y., Wang, G., Zhong, L., Liao, W., Wang, J., & Liao, Y. (2024). Analysis and validation of high-power laser machining with variable defocus for thick steel plates without assistant gas. Optics and Lasers in Engineering, 181, 108353.

[14] Liao, W., Wang, G., Zhong, L., Chen, Y., & Wang, J. (2024). Feasibility analysis and cutting process research on laser cutting medium-thick 20CrNiMo steel plates using a high-power fiber laser without assisted blowing. Journal of Manufacturing Processes, 111, 130-138.

[15] Wandera, C., & Kujanpää, V. (2011). Optimization of parameters for fiber laser cutting of a 10 mm stainless steel plate. Proceedings of the Institution of Mechanical Engineers, Part B: Journal of Engineering Manufacture, 225(5), 641-649.

[16] Manohar, M., Bodnar, R. L., Asfahani, R. I., Chen, N., & Huang, C. (2005). Effect of steel composition on the laser cutting behavior of 25-mm-thick plates. Journal of Laser Applications, 17(4), 211-218.

[17] Tamura, K., Ishigami, R., & Yamagishi, R. (2016). Laser cutting of thick steel plates and simulated steel components using a 30 kW fiber laser. Journal of Nuclear Science and Technology, 53(6), 916-920.

[18] Liu, Y., & Zhang, S. (2024). Improving the cutting process and quality of thick plates with high-power fiber laser. Optical Fiber Technology, 83, 103684.

[19] Wang, Y., Li, Z., Wei, X., Jing, X., Yang, F., Li, Y., & Zhang, X. (2025). Finite element simulation and experimental verification of laser machining of nitinol tubes. Optics & Laser Technology, 181, 111672.

[20] Vora, H. D., Santhanakrishnan, S., Harimkar, S. P., Boetcher, S. K., & Dahotre, N. B. (2013). One-dimensional multipulse laser machining of structural alumina: evolution of surface topography. The International Journal of Advanced Manufacturing Technology, 68(1), 69-83.

[21] Parandoush, P., & Hossain, A. (2014). A review of modeling and simulation of laser beam machining. International journal of machine tools and manufacture, 85, 135-145.

[22] Faraji, A. H., Maletta, C., Barbieri, G., Cognini, F., & Bruno, L. (2021). Numerical modeling of fluid flow, heat, and mass transfer for similar and dissimilar laser welding of Ti-6Al-4V and Inconel 718. The International Journal of Advanced Manufacturing Technology, 114(3), 899-914.

[23] Singh, G., Teli, M., Samanta, A., & Singh, R. (2013). Finite element modeling of laser-assisted machining of AISI D2 tool steel. Materials and manufacturing processes, 28(4), 443-448.

[24] Cepauskaite, L., & Bendikiene, R. (2024). Effect of Fiber-Laser Parameters on Cutting Accuracy of Thin and Thick S355JR Structural Steel Plates. Metals, 14(6), 723.

[25] Buj-Corral, I., Costa-Herrero, L., & Domínguez-Fernández, A. (2021). Effect of process parameters on the quality of laser-cut stainless steel thin plates. Metals, 11(8), 1224.

[26] Pramanik, D., Kuar, A. S., Sarkar, S., & Mitra, S. (2020). Effects of Cutting Angle on Multiple Quality Characteristics for the Microcutting of Thin 316L Stainless Steel Using a Low Power Fiber Laser. Lasers in Engineering (Old City Publishing), 45.